

Connecting Particle Fracture with Electrochemical Impedance in $\text{Li}_x\text{Mn}_2\text{O}_4$

To cite this article: Frank P. McGrogan *et al* 2017 *J. Electrochem. Soc.* **164** A3709

View the [article online](#) for updates and enhancements.



Connecting Particle Fracture with Electrochemical Impedance in $\text{Li}_x\text{Mn}_2\text{O}_4$

Frank P. McGrogan, Sean R. Bishop,* Yet-Ming Chiang, and Krystyn J. Van Vliet^z

Department of Materials Science & Engineering, Massachusetts Institute of Technology, Cambridge, Massachusetts 02139, USA

Li-ion battery (LIB) electrodes subjected to repeated electrochemical cycling exhibit limited lifetime and gradual performance loss. Fracture of the active electrode particles, though one of the most widely discussed degradation mechanisms, is still not understood fully in even the most studied positive electrode systems. Here, we develop the connection between fracture and impedance in $\text{Li}_x\text{Mn}_2\text{O}_4$ composite electrodes via cycling schedules designed to produce discrete fracture events. We establish a correlation between these fracture events and acoustic emissions, as well as a parallel correlation between acoustic emissions and impedance growth. Through extensive impedance analysis, including conversion of impedance data to distributions of relaxation times, we identify the sources of impedance growth as electronic contact impedance and ionic surface layer impedance. Through measurements at multiple temperatures, we also estimate activation energies of ~ 0.1 eV for electrolyte resistance, bulk contact resistance, and current collector resistance, ~ 0.4 eV for charge-transfer resistance, and ~ 0.3 eV for cathode surface layer resistance. We thus demonstrate a direct and correlative relationship between electrochemomechanical fatigue and performance loss, which can inform LIB design and characterization for improved longevity and late-life performance.

© 2017 The Electrochemical Society. [DOI: 10.1149/2.0941714jes] All rights reserved.

Manuscript submitted September 14, 2017; revised manuscript received October 31, 2017. Published December 6, 2017.

Dependable and affordable energy storage is critical to the wider adoption of intermittent renewable energy sources and electric vehicles. Currently available Li-ion batteries (LIBs) exhibit sufficient energy and power density for many of these applications, but inadequate battery lifetime and poor late-life performance remain persistent obstacles to electrochemical storage strategies.^{1,2} As a result, extensive research has focused on identifying and eliminating the dominant mechanisms of capacity fade and impedance growth in LIBs, including fracture of the electrochemically active particles within electrodes. This fracture is generally considered to be detrimental to electrochemical performance via several potential mechanisms. As shown in Fig. 1, these mechanisms include electrode fragmentation and electronic isolation,³⁻⁶ disruption of ionic diffusion,⁷ acceleration of transition metal dissolution and electrolyte decomposition,⁸ and the consumption of Li into solid electrolyte interphases (SEI).^{3,9}

These degradation mechanisms are plausible, discussed widely, and modeled frequently. However, a direct link between particle fracture and performance loss remains elusive in many systems due to concurrent chemical and mechanical deterioration in virtually all situations in which fracture has been observed. Our groups and others have shown that particle fracture is concentrated heavily in the first one to two charge and discharge cycles¹⁰⁻¹⁴ (i.e., conditioning or formation cycles). As many other transient chemical reactions are taking place during these initial cycles, it is difficult to isolate the effects of fracture at this time scale. Others have convincingly demonstrated extensive particle fracture associated with certain cycle numbers later in the life of the battery, and have shown that cycling conditions such as range of operating voltage can influence the degree of fracture after repeated cycling.^{15,16} However, such post mortem observations do not isolate the timing of the fracture or the relative contribution of fracture to the observed performance loss as a function of time. Moreover, demonstrations of improved capacity via engineered mechanical behavior (e.g., by doping or adding surface layers) typically result from a combination of mechanical stability and improved surface chemistry.¹⁷⁻²² Here, we aimed to test the link between fracture and impedance growth by triggering discrete fracture events in $\text{Li}_x\text{Mn}_2\text{O}_4$ (LMO) positive electrodes at defined intervals during stable cycling, thus facilitating identification of any strong temporal correlations between fracture and electrochemical performance.

To control the occurrence of fracture in a Li-ion battery electrode, a working understanding of its electrochemically-driven fracture mechanisms is required. Fracture-inducing chemomechanical stresses arise from multiple contributors in LIBs, including phase transformations,^{16,23,24} anisotropic chemical expansion coefficients,^{10,25,26} and “diffusion-induced stress” (DIS) caused by transient Li-ion concentration gradients.²⁷⁻²⁹ For the purpose of the present study, DIS is the simplest to control because this stress increases with increasing applied charge rate (C-rate). As shown in the detailed spherical electrode particle models of Woodford et al.,²⁷ smaller particles require higher C-rates to induce unstable crack propagation. Therefore, in a composite electrode containing a wide distribution of particle sizes, intact particles exist even after mechanical damage has been effectively saturated at a given C-rate. Further increases in C-rate then lead to fracture in smaller particles. This functional dependence of fracture on applied C-rate provides a convenient lever for controlling the timing of fracture by electrochemical means.

For several reasons described below, we selected the LMO spinel positive electrode as the test material for C-rate-controlled fracture implementation. Most importantly, LMO and its doped derivatives exhibit significant capacity fade, and many studies have identified the primary culprit as dissolution of Mn into the electrolyte.³⁰⁻³⁸ This dissolution becomes more severe at high temperatures and at extreme potentials, but the influence of fracture is not clear. Also critical to our study of LMO is the thorough characterization of its phase transformation behavior and predictive modeling of cycling-induced stress available in the literature. In the normal cycling range ($0 < X < 1$) for $\text{Li}_x\text{Mn}_2\text{O}_4$, stress evolution occurs from the combined effects of DIS and cubic-cubic phase transformations, as accounted for in the electrochemical shock model of Woodford et al.²³ and measured in situ by Sheth et al.³⁹ At low voltage and high levels of lithiation ($1 < X < 2$), a highly anisotropic phase transformation associated with the Jahn-Teller effect occurs, but the resulting tetragonal spinel phase can also be found within the normal cycling range as a result of inhomogeneous discharge.^{40,41} Knowledge of this complex phase behavior is necessary for the accurate interpretation of our fracture and electrochemical data. Finally, the detailed studies of impedance spectra for LMO and related spinels available in the literature aid our analysis of the complex impedance responses to fracture shown herein.⁴²⁻⁴⁵

In this study, we combined the advantages of both mechanical and electrochemical characterization techniques, so that we could induce fracture events and concurrently monitor any detectable changes in electrochemical performance. We monitored fracture during cycling with an acoustic emissions sensor, and confirmed the occurrence of widespread fracture in the electrodes via post mortem scanning electron microscopy. Additional acoustic activity occurred during periods of elevated C-rate, consistent with intensification of fracture conditions. We also tracked electrochemical impedance as a function of

*Electrochemical Society Member.

^zE-mail: krystyn@mit.edu

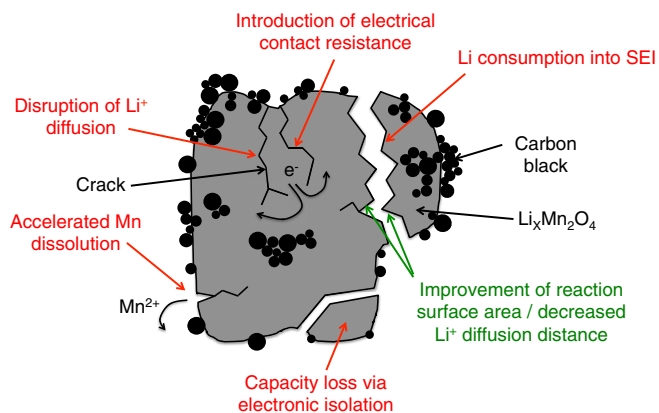


Figure 1. Potential mechanisms by which fracture may affect the performance of an electrode, considering $\text{Li}_x\text{Mn}_2\text{O}_4$ as an example active material within a composite positive electrode. Harmful mechanisms (red) include disruption of ion and electron flow, as well as the acceleration of transition metal dissolution. For negative electrodes, the consumption of active Li through solid electrolyte interphase (SEI) formation results in capacity fade. On the other hand, increase of electrochemically active surface area (green) may also have a beneficial effect on electrochemical performance at shorter time scales.

time during cycling, and observed an increase in impedance that correlated temporally with the induction of fracture. By testing the LMO impedance spectrum under varied conditions and applying distribution of relaxation time (DRT) analysis, we associated these impedance increases with a cathode surface layer and electronic contact resistance. The simultaneous observation of isolated fracture and concurrent impedance growth provides a critical correlation for LMO electrodes, and outlines a previously unexplored path for understanding the fractured-based mechanisms of capacity loss.

Methods

Sample fabrication.—Composite electrode films containing LiMn_2O_4 powder in a carbon/binder matrix cast on aluminum foil were purchased from MTI Corporation (Richmond, CA) and punched into discs of 12 mm diameter. Film thickness of 85 μm and active material percentage of 94.2 wt% were specified by the manufacturer. The resulting average active mass per 12 mm electrode was ~ 16 mg LMO. $\text{LiMn}_2\text{O}_4/\text{Li}$ half-cells were assembled in an Ar-filled glovebox using 2032 coin cell hardware (MTI Corporation, Richmond, CA) with a wave spring, spacer, Li metal foil counter electrode (Alfa Aesar), and two separator layers (Tonen; Minatoku, Tokyo, Japan). The cells contained approximately 0.2 mL of electrolyte solution comprising 1.2 M LiPF_6 in a 1:1 (by volume) mixture of ethylene carbonate and diethyl carbonate. In separate control experiments, electrodes (LiMn_2O_4 , $\text{LiNi}_{0.5}\text{Mn}_{1.5}\text{O}_4$, and silicon) were produced in-house, using procedures detailed in Supplementary Material (SM), S1; the corresponding cell assembly procedure was the same as that described above.

Electrochemical testing.—Application of electrochemical shock theory.—Discrete fracture events were created and controlled with an “electrochemical shock map” approach, as shown schematically in Fig. 2a. Woodford et al.²³ computationally produced such maps predicting the critical C-rate for fracture as a function of particle size for DIS and the cubic-cubic phase transformation of LMO. Starting with a composite electrode containing a distribution of particle sizes (indicated at the bottom of the figure), fracture occurs over a distribution of critical C-rates in the electrode. At a given C-rate, particles to the right of the fracture boundary (i.e., larger particles) fracture to create effectively smaller particles which may then fall to the left of the fracture boundary. This trend can eventually saturate the mechanical damage at that C-rate. Increasing the C-rate for a full cycle (i.e., a

“C-rate spike” as indicated in this figure) effectively positions smaller particles beyond the fracture boundary, causing additional fracture to occur.

As shown schematically in Fig. 2b, the strategy that we adopted in this work was to repeatedly expose the electrode particles to higher C-rates in step-like sequences termed “C-rate spikes,” while closely monitoring the electrochemical impedance of the battery. We aimed to determine whether correlations existed between fracture detection and electrochemical impedance changes under the conditions used in these experiments.

Galvanostatic cycling and electrochemical impedance spectroscopy (EIS).— $\text{Li}_x\text{Mn}_2\text{O}_4$ electrodes were cycled using a Solartron 1470E tester at a base rate of $\sim C/5$ from 2.8 V – 4.5 V. This wide voltage window was chosen to allow more consistent charge and discharge completion at high C-rates, which were accompanied by increased overpotentials, while simultaneously protecting the electrode from extensive electrolyte oxidation (high voltage) or Jahn-Teller effect (over-discharge). The cells rested at open circuit for 45 minutes after momentarily reaching these potential limits, typically relaxing to ~ 4.2 V and ~ 3.8 V after charging and discharging, respectively. After each open circuit segment, the potential was fixed at the final open circuit voltage of that step, and an impedance measurement was conducted. The applied sinusoidal amplitude was 10 mV, and data were collected at 10 points per decade between 1 MHz and 0.01 Hz. The next galvanostatic step began immediately after completion of each impedance measurement.

Starting from the baseline C-rate, variations in C-rate were applied according to the schedules outlined in Table I. Acoustic emissions were measured during these cycling experiments as described in the following section.

Separate impedance characterization experiments were conducted to separate overlapping time constants via temperature and state-of-charge variation. For the state-of-charge experiments, the cell potential was adjusted in the decreasing voltage direction at a rate of $-50 \mu\text{V/s}$ between impedance collection points. Before each impedance measurement, the cell was held at constant potential for 11 h or for 1 h after the current decayed below 5 μA . For temperature-dependence experiments, impedance data were collected on a Solartron ECS Modulab impedance analyzer with 10 mV sinusoidal bias amplitude and 15 points per decade between 1 MHz and 0.1 Hz. Temperature was modulated using a resistive heating pad connected in series with a variable transformer and temperature controller, with a J-type thermocouple mounted on the positive electrode side of the coin cell. Measurements below room temperature were conducted with the cell and resistive heating pad placed in an insulated container filled with ice. Additional impedance characterization studies beyond temperature and state-of-charge variation are described in SM, S2-5.

Acoustic emissions measurements.—Acoustic emission measurements were conducted using a Physical Acoustics Corp. (Princeton Jct, NJ) instrument controlled by AEWIn software. Signals were collected with a Micro30 Medium Frequency Miniature Sensor (PAC, Princeton Jct, NJ) connected to a 2/4/6 voltage pre-amplifier set to 60 dB gain. The sensor was attached to the positive electrode side of the coin cell using vacuum grease and rubber bands to maximize acoustic coupling. In order to distinguish sensor response from ambient noise, software settings were adjusted to register only acoustic events with at least three wave cycles above a threshold of 23 dB. Additionally, software filters were applied to create a bandpass between 100 kHz and 2 MHz. Signal-to-noise tests were conducted periodically to ensure that ambient laboratory noise was not mischaracterized as acoustic emissions. Electromagnetic interference caused by channel switching in the impedance equipment was identified by time of occurrence and waveform characteristics, and was removed during post-processing of data. Further waveform characteristics used to identify the sources of acoustic emissions were compared to the silicon control experiment, as detailed in SM, S6.

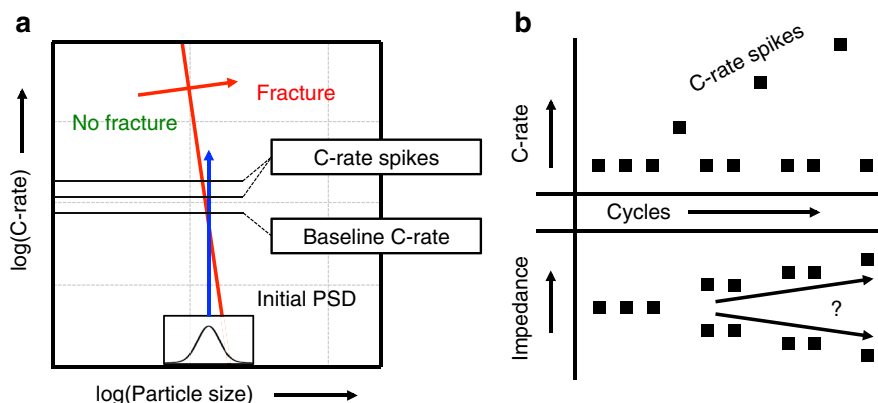


Figure 2. a) Schematic electrochemical shock map as calculated by Woodford et al.²³ for a two-phase $\text{Li}_x\text{Mn}_2\text{O}_4$ particle. An initial particle size distribution (PSD) is projected across the fracture boundary to demonstrate additional fractures predicted for C-rate spikes. b) Illustration of C-rate spikes and the impedance response. The effect of fracture on the impedance is determined from the impedance response following C-rate spikes.

Scanning electron microscopy.—Scanning electron microscopy (SEM) was conducted on a Zeiss Merlin High-Resolution SEM to confirm whether fracture consistent with electrochemical shock had occurred in the cycled material. The cycled battery (Cell A) was opened in an Ar-filled glovebox using a specialized opening tool to prevent shorting of the coin cell. The cathode was rinsed with diethyl carbonate to remove excess electrolyte salt. The cycled $\text{Li}_x\text{Mn}_2\text{O}_4$ electrode and a pristine electrode were then analyzed via SEM in the following manner. For each electrode, 30 particles were first selected by the researcher while imaging the sample at sufficiently low magnification that cracks could not be resolved, to minimize user bias. Particles of approximately 10 μm or greater in diameter were chosen to ensure consistent likelihood of electrochemical shock in the particles. After each particle selection at low magnification, the magnification was increased to 8000X and a high-resolution image was acquired. The high-resolution images were then used to identify fractured particles. Examples of fractured and unfractured particles are provided in SM, S7.

Impedance analysis methods – Distribution of relaxation times (DRT) analysis.—In Li-ion batteries, impedance spectra can typically be modeled with equivalent electronic circuits composed of a finite number of R||CPE (a resistor in parallel with constant phase element, the latter representing capacitance) elements in series and a Warburg diffusion element at the low frequency end of the spectrum.^{46,47} The R||CPE contributions can be distinguished if there exists sufficient difference between the time scales of each contribution (i.e., if the relaxation times of the R||CPE elements are well separated), as is often the case for geometrically well-defined thin films. Because commercial composite LIB electrodes typically consist of complex geometry and multiple types of material interfaces, relaxation times vary spatially for each contribution, causing distortion of the corresponding semicircles in the complex plane. Furthermore, multiple contributions may have similar relaxation times, leading to the convolution of impedance signals.⁴⁴ As described below, use of distribution of relaxation times (DRT) analysis yields superior visual resolution of overlapping impedance signals, as compared to the conventional complex plane representation.

In the DRT approach, the electrochemical cell is viewed as a series of infinitely many RC (resistor and capacitor in parallel) elements, as shown in Fig. 3, with a single resistor R_0 to represent the ohmic

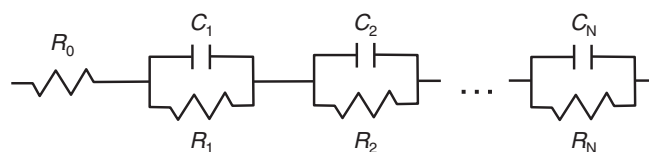


Figure 3. General equivalent circuit for a Li-ion battery. Infinitely many RC circuit elements in series can be expressed as a distribution of relaxation times.

(in-phase) current response at high frequency. Each RC element is described by impedance $Z_k = R_k / (1 + j\omega R_k C_k)$, so that the entire cell impedance can be written in the following general form:^{48–50}

$$Z(\omega) = R_0 + Z_{pol}(\omega) = R_0 + \sum_{k=1}^N \frac{R_k}{1 + j\omega R_k C_k} \quad [1]$$

where ω is 2π multiplied by the frequency of the applied sinusoidal bias, and the subscript “pol” indicates the polarization, or electrode, contribution. N is a large number, and in the present case is equal to the total number of data points collected in each impedance spectrum. Taking τ_k as the time constant equal to $\tau_k = R_k C_k$ for each RC element, and introducing a distribution of relaxation times γ_k , the impedance can be rewritten as

$$Z(\omega) = R_0 + R_{pol} \sum_{k=1}^N \frac{\gamma_k}{1 + j\omega \tau_k} \quad [2]$$

where R_{pol} is the polarization resistance. After expressing the impedance in terms of DRT, the rest of the analysis consists of solving Eq. 2 for γ_k . The method employed in this work involves expressing the imaginary impedance as a convolution equation and solving numerically with Fourier transforms, as described by Schichlein et al.⁴⁸ In the resulting spectrum, R_{pol} times the area of each peak is equal to the total resistance associated with the corresponding impedance contribution.

The equivalent circuit in Fig. 3 is useful specifically as a general model for impedance features with semicircular shapes (R||CPE) in the complex plane representation. Since Li-ion battery impedance also contains the divergent Warburg diffusion feature at low frequency, fitting and subtraction techniques were used when possible to remove this feature, thereby allowing the complex plane data to converge to the real axis at low frequency. As a result, only impedance components of

Table I. List of samples and C-rate variations for cycling experiments.

	Cell A	Cell B	Cell C
Sequences before C-rate spikes	-	-	11 cycles + temperature dependence
Baseline C-rate	C/5	C/5	C/5
C-rate spike current multiplier (cycle within C-rate spike sequence)	x2 (21), x3 (27), x4 (33)	x2 (8), x3 (12)	x2 (6), x3 (12)
Acoustic emissions monitored	Yes	No	Yes
Impedance monitored	Yes	Yes	Yes

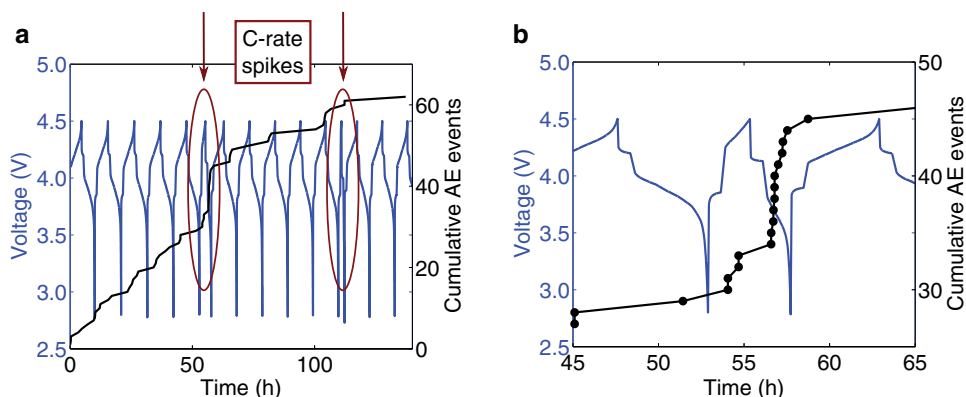


Figure 4. a) Cumulative acoustic emissions (black line) as a function of time for Cell C, with cyclic voltage curves (blue lines) superimposed. Locations of temporarily increased C-rate (i.e., C-rate spikes) are indicated by arrows. Results are reported following 11 conditioning cycles. b) Acoustic response and voltage curve for the first C-rate spike shown in (a).

the R||CPE form – semicircular features with time constants between 10^{-1} Hz and 10^5 Hz – were investigated by DRT. In some cases, the subtraction was not possible but the noise features could be identified visually. Finally, numerical filtering was applied to the Fourier transform of the DRT to remove noise features caused by amplification of experimental error. Details of the solving, fitting, subtraction, and numerical filtering techniques are described in more detail in SM, S8.

After identification of the number of peaks and associated time constants with DRT analysis, quantitative values of resistance were evaluated either by conducting CNLS (complex nonlinear least squares) fitting in ZView (Scribner, Southern Pines, NC) software or by fitting Gaussian functions to the DRT in MATLAB (The MathWorks, Natick, MA).

Materials characterization by spectroscopic methods.—Post mortem comparisons of cycled (Cell B) and uncycled $\text{Li}_x\text{Mn}_2\text{O}_4$ electrodes were conducted using energy-dispersive X-ray spectroscopy (EDS) and X-ray photoelectron spectroscopy (XPS). The Li metal counter electrodes used in Cell B were also analyzed with both spectroscopic techniques.

EDS was conducted on an FEI/Philips XL-30 SEM with an EDAX Super Silicon Drift Detector, using accelerating voltages between 7 kV and 15 kV to enable the observation of Mn on the Li anode. The spectra were analyzed using the Point Analysis tool on TEAM (AMETEK, Berwyn, PA) software.

XPS was conducted on a Physical Electronics Versaprobe II X-Ray Photoelectron Spectrometer with reported depth resolution of less than 10 nm. Binding energies were corrected using the carbon signal at 289.5 eV as an internal standard. All fitting was conducted in the CasaXPS software. Survey spectra were collected over the full range of 0 to 1100 eV, and high-resolution spectra were taken in the vicinity of the C1s and Mn2p peaks. The XPS was used to investigate changes in Mn oxidation state on the surface of the cathode, as well as the presence of Mn on the Li anode. All samples were transferred from the glovebox to the XPS equipment using an airtight transfer vessel.

The results of the EDS and XPS experiments are reported in SM, S9.

Results

Correlation of fracture with acoustic emissions.—To test for correlations between LMO particle fracture and acoustic emissions, we conducted in situ measurements of acoustic emission events during cell cycling, and subsequently analyzed the electrode materials post mortem to compare with uncycled counterparts. As discussed below, fractography and design of cycling sequences aided our isolation of LMO particle fracture as the primary source of detectable acoustic emission events, as opposed to other acoustic signals that could potentially occur during in situ measurements.

Acoustic emissions during galvanostatic cycling.—All cells exhibited acoustic emissions during galvanostatic cycling. Each cell was cycled several times before beginning the C-rate spikes to bypass the anomalous changes in capacity and impedance commonly observed in the conditioning cycles. As shown in Fig. 4a, cycling of Cell C at C/5 continued for ~ 53 h (5 cycles) following a preliminary cycling sequence consisting of 11 cycles at C/5 and subsequent testing of impedance temperature dependence, as described below and indicated in Table I. During these first 5 cycles at baseline C-rate in Fig. 4a, acoustic emission events were observed at an approximately constant rate, as indicated by the linear increase in cumulative acoustic emissions with time. For the sixth cycle, the applied current was doubled (i.e., C-rate spike), and an enhanced acoustic response was observed. This enhanced signal is consistent with the expectation that electrochemical shock-induced fracture of LMO occurs with increased C-rate.

Fig. 4b shows that acoustic emissions occurred primarily in the discharge (~ 4.0 to 2.8 V) and early charge (4.2 to 4.5 V) phases of the cycle. After the C-rate spike, the rate of acoustic emissions accumulation dropped to a magnitude lower than the initial rate. After five additional cycles at C/5, the C-rate was tripled, and another but weaker acoustic response was observed. Similar acoustic responses to C-rate spikes were reproduced successfully and independently in Cell A. An acoustic response consistent with electrochemical shock criteria was also produced by C-rate ramping in a $\text{Li}_x\text{Ni}_{0.5}\text{Mn}_{1.5}\text{O}_4$ cell, confirming reproducibility; more details on results from these other cells are given in SM, S10. As expected, in all cases, the first one to two cycles applied to the fresh cell during the conditioning stage produced many acoustic events (not shown), consistent with previous studies in electrochemical shock, and these events were typically an order of magnitude more numerous than in subsequent C-rate spikes.

Post mortem microscopy and analysis of cycled material.—Statistical analysis of SEM images of $\text{Li}_x\text{Mn}_2\text{O}_4$ particles was conducted for the cycled Cell A electrode and compared with uncycled electrode material. Figure 5 shows an example of a crack network found in the cycled material, indicating cracks with red arrows. The cycled electrode exhibited cracking consistent with electrochemical shock, with 60% of the imaged electrode particles fractured. The physical locations of these particles on the composite electrode, as well as the portion of the cycled electrode used for the analysis, are illustrated in the inset of Fig. 5. The cracks typically appeared thin, straight, and deep, often branching to form a network of cracks in the particle with crack-to-crack spacing on the order of 1–3 μm , and the crack networks usually extended through most of the visible volume of the particle. For the uncycled cathode material, $< 10\%$ of the particles exhibited flaws that were similar in appearance to crack networks in the cycled particles. This comparison supports the role of electrochemical cycling in

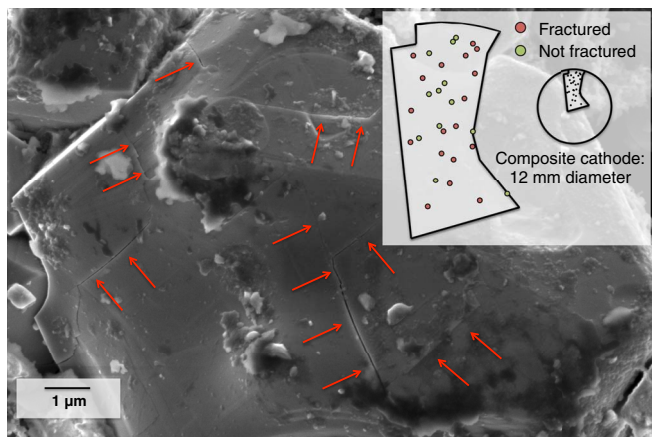


Figure 5. Scanning electron micrograph of fracture network in $\text{Li}_x\text{Mn}_2\text{O}_4$ resulting from electrochemical cycling. Locations of fractured and unfractured particles imaged on a piece of cycled $\text{Li}_x\text{Mn}_2\text{O}_4$ composite cathode (Cell A) using a statistical approach are shown in the inset.

promoting active particle fracture under these conditions. An additional control cell, cycled without C-rate spikes, exhibited cracking characteristics similar to Cell A (SM, S11). This second comparison confirms that appreciable fracture can also be detected by acoustic emissions in the absence of C-rate spikes at the same baseline C-rate. Exclusion of other types of surface flaws from the SEM electrochemical shock analysis is discussed in SM, S7.

Correlation of impedance with acoustic emissions.—Having established correlation between fracture and the in situ surrogate of acoustic emissions, we next considered operando correlations between this fracture surrogate and functional consequences to battery performance. To test for correlations specifically between electrical impedance and acoustic emissions, we measured and analyzed impedance spectra on a twice-per-cycle basis, including immediately before and after implementation of C-rate spikes. As discussed below, these comparisons demonstrated a strong correlation between impedance growth and acoustic emission accumulation. While both acoustic emissions and impedance growth occurred gradually over each cycle, sudden and more significant increases in both quantities occurred during the applied C-rate spikes.

Changes in impedance following C-rate spikes.—During steady-state cycling at constant C-rate, the total electrochemical impedance increased gradually each cycle. Following each C-rate spike, sudden increases in the total electrochemical impedance occurred that were significantly larger than those expected from steady-state cycling. Fig. 6a demonstrates this effect for Cell B in the complex plane, with impedance spectra shown for cycles 5–7, 9–11, and 13–15 in the discharged state, all following full discharges at C/5 and open circuit segments of 45 minute duration. Cycles 8 and 12 correspond to C-rate spikes of C/2.5 and C/1.7, respectively, resulting in a different state of charge after open circuit conditions (data not shown). Each impedance spectrum consisted of a high frequency offset on the real axis (left side of figure), followed by distorted semi-circles at high and middle frequencies, and ultimately a diffusive “tail” at the lowest frequencies (right side).

We assigned spectrum features based on previous studies and our own experiments at different temperatures, electrode compositions, and cycling histories. Generally, the ohmic resistance at the high frequency offset is consistent with ionic transport resistance through the electrolyte and separator ($\sim 10 \Omega$).^{43,46} Thus, we assigned the high frequency offset to the electrolyte, as assumed commonly by others. From these data, we calculated the activation energy for the electrolyte resistance as 0.15 eV, similar to previous reports.^{43,47} As discussed below, we attributed the intermediate frequency response (characterized

by convoluted depressed semicircles) to the interfacial components of the electrode resistance; this group of features exhibited an increase in resistance following each C-rate spike. The lowest frequency “tail” is commonly assigned to bulk diffusive processes within the electrode or electrolyte and is not discussed further herein.^{44,46} Since multiple arcs in the electrode impedance spectra overlapped significantly, and were therefore difficult to deconvolute visually, we employed DRT analysis of the intermediate frequency region between 10^{-1} Hz and 10^5 Hz.

DRT analysis improved the identification of separate impedance contributions, as shown in Fig. 6b. While only two overlapping semi-circles were obvious from visual inspection of the impedance spectra, the peaks shown by DRT analysis included at least three features. We multiplied the DRT by R_{pol} such that the area of each peak represented the total resistance of the corresponding impedance contribution(s). Therefore, we could compare the area of each peak, not only within each spectrum, but also among multiple spectra (i.e., across the spectra corresponding to each cycle), each with differing total areas.

Figure 6b shows that sudden increases in peak height were visible after the C-rate spikes for the rightmost peak at ~ 600 Hz and for a middle-frequency peak emerging at ~ 16 Hz. We conducted peak area calculations by fitting Gaussian functions to the peaks as described in SM, S12. Figure 6c shows that the fitted peak areas, and therefore resistances, of both the 600 Hz and 16 Hz impedance contributions increased as a result of the C-rate spikes. The ohmic (high-frequency) impedance also increased during the C-rate spikes, as fit by ZView. While the peak at 4 Hz was difficult to fit reliably, decreases in this low-frequency feature were visible after the first C-rate spike. This analysis demonstrates the usefulness of the DRT in separating impedance growth contributions, as it enables the observation of multiple impedance changes corresponding to time constants occurring within one order of magnitude.

Characterization of electrochemical impedance spectra.—Variation of temperature and state-of-charge enabled location and deconvolution of the DRT peaks. Fig. 7a shows four distinct impedance processes that we identified while varying temperature between 4°C and 48°C in increments of $\sim 5^\circ\text{C}$ in Cell B. The peak labeled * is excluded from discussion, as it was an artifact of DRT conversion and thus was not included in the ZView calculations used here. As peak β only dominates at high temperature, and Peaks χ and δ are separated only at low temperature, exploration of this entire temperature range was necessary to characterize the impedance peaks present at room temperature. We observed a similar temperature profile in Cell C, and applied ZView fitting to data both from Cells B and C to determine the activation energies for peaks α , β , χ , and δ as 0.38 eV, 0.05 eV, 0.34 eV, and 0.14 eV, respectively. We studied peaks α , β , and χ from Cell C due to good separation of these processes over a wide temperature range. Figure 7b shows how we used a single middle-frequency peak fit for peaks β and χ , as it exhibited distinct thermal behaviors at high and low temperature. The activation energies calculated from Cell C were used as input constraints to enable the fitting of peak δ in Cell B. Figure 7c shows the resulting activation energy for peak δ . Additional details of this fitting process and the possible sources of error are provided in SM, S13.

We also measured the state-of-charge dependence of impedance on a similar $\text{Li}_x\text{Mn}_2\text{O}_4/\text{Li}$ cell after 1.5 cycles at C/5. Figure 8 shows a convolution of peaks β , χ , and δ that nearly tripled in total resistance as the potential was decreased from 4.3 V to 3.8 V. At low frequency, peak α was dominant only at potentials < 4.0 V and > 4.2 V, consistent with charge-transfer resistance. We describe the assignments of physical impedance contributions to these four peaks, and the implications for electrochemically induced particle fracture, in the Discussion.

Discussion

Fracture correlation with C-rate spikes.—Microscopic comparison of cycled and uncycled cathodes via SEM confirmed that electrochemical cycling under these conditions resulted in significant particle

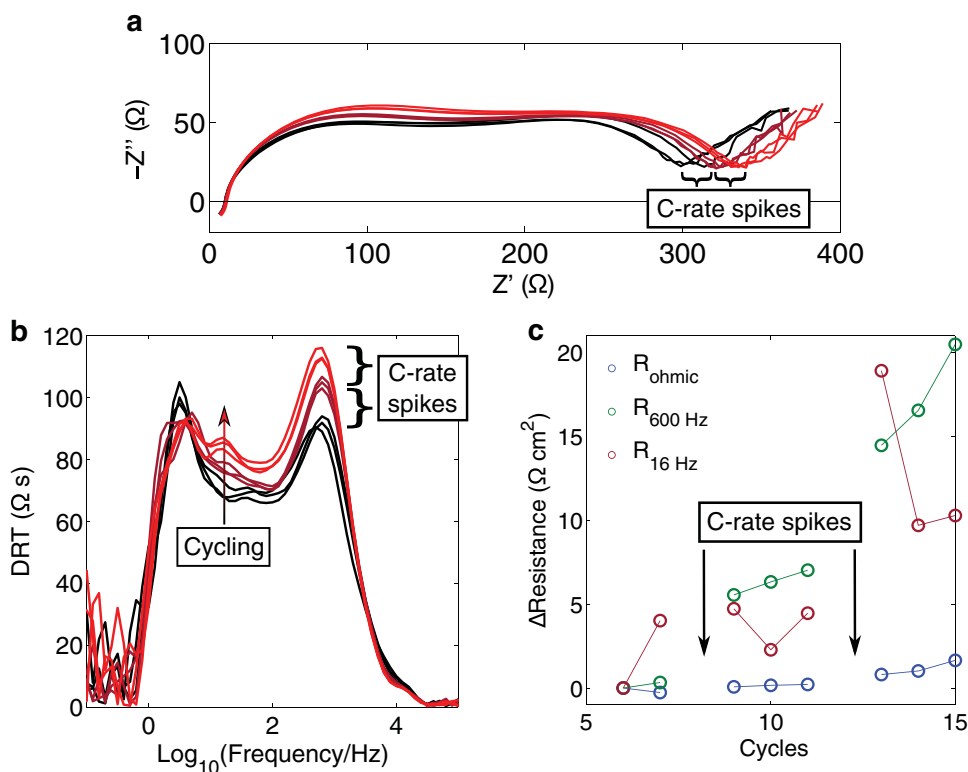


Figure 6. Electrochemical impedance analysis. a) Complex plot of electrochemical impedance for three cycles before C-rate spikes (black), after the first C-rate spike (dark red), after two C-rate spikes (bright red). b) Distribution of relaxation times representation of impedance changes after these C-rate spikes. Resistance decreases for the peak at 4 Hz, but increases for the peaks at 16 Hz and 600 Hz. c) Resistance increases at the C-rate spikes for the impedance peaks at 600 Hz and 16 Hz, as calculated from the distribution of relaxation times via Gaussian fitting. Increases in the high-frequency intercept (R_{ohmic}) also occur at the C-rate spikes.

fracture. The in situ acoustic emissions reported in Fig. 4 exhibit several important features consistent with electrochemical shock. Most importantly, the acoustic response was sensitive to applied C-rate, as more acoustic emissions were registered during the C-rate spikes. Simulated electrochemical shock maps by Woodford et al.²³ predict C/5 cycling to cause fracture in particles exceeding $\sim 2 \mu\text{m}$ diameter. In our experiments, the starting particle size distribution (PSD) included a range of particle sizes from the submicron range to $> 10 \mu\text{m}$. The SEM images revealed crack spacing of $\sim 1\text{-}3 \mu\text{m}$ on large particles, as in Fig. 5. This finding suggests that our PSD spans both above and below the C/5 fracture criterion predicted by the electrochemical shock map, enabling us to probe the effects of C-rate sensitivity.

As mentioned previously, we observed widespread fracture in another electrode exhibiting acoustic emissions that was not subjected to C-rate spikes (SM, S11). Thus, we attribute acoustic emissions during both baseline cycling and the C-rate spikes to particle fracture. The acoustic emissions recorded during some C-rate spikes (e.g., Fig. 4, second C-rate spike) were not noticeably different from the acoustic patterns during baseline cycles. This variable amplitude of acoustic emission responses to C-rate spikes is consistent with fracture as a stochastic event, and with the high variance associated with small numbers of acoustic signals (only ~ 60 total acoustic emissions in Fig. 4). Further, the modest accumulation of fracture events detected during baseline cycling is consistent with electrochemomechanical fatigue damage progression, whereby fracture may accumulate slowly due to changing morphological and electrochemical boundary conditions (e.g., newly formed particle surfaces and/or modified lithiation kinetics) even after initial electrochemical shock.

While fracture of electrochemically active electrode particles was the most likely cause of the observed acoustic emissions, we also considered other potential sources of acoustic emissions such as binder delamination or gas evolution from side reactions. To ensure that the acoustic emissions did not correlate simply with the total charge

passed, we graphed the cumulative acoustic emission curves as a function of cumulative capacity rather than time. The sudden increases in acoustic emission rate still appeared prominent in the high current region associated with the C-rate spike (see SM, S14). Additionally, we cycled one cell repeatedly at C/2.5 after the reported C-rate spike sequence, with minimal increase in the baseline rate of acoustic emissions (see SM, S15). This absence of increase in baseline acoustic response is consistent with our understanding of electrochemical shock, as C-rate dependent fracture has been shown to saturate quickly during cycling at constant C-rate.¹⁰⁻¹⁴

The potential conditions under which acoustic emissions were observed did not match conditions expected to promote electrolyte oxidation reactions. Acoustic emissions due to side reactions (e.g., gas evolution during electrolyte decomposition) were observed clearly in a $\sim 5 \text{ V}$ $\text{Li}_x\text{Ni}_{0.5}\text{Mn}_{1.5}\text{O}_4$ composite electrode as the potential exceeded $\sim 4.8 \text{ V}$, consistent with oxidation conditions for organic liquid electrolytes^{45,51} (see SM, S10). In contrast, the $\text{Li}_x\text{Mn}_2\text{O}_4$ electrodes herein were not exposed to potentials exceeding 4.5 V , and the observed acoustic emissions were not prevalent at potentials approaching 4.5 V . The acoustic emissions in Fig. 4 occurred instead at potentials expected to promote LMO cubic-cubic phase transformation events, concurrently with the voltage plateaus.^{52,53} The electrochemical shock fracture boundary in Fig. 2a is dictated by contributions from both phase transformation stress and C-rate dependent stress arising from Li gradients within a given particle. Therefore, the total chemomechanical stress is maximized in the two-phase regime and acoustic emissions and fracture are expected to occur in this regime.⁵⁴ However, despite these consistencies with fracture in the cubic-cubic two-phase regime, the experiments herein cannot completely rule out the influence of small amounts of tetragonal phase that could promote fracture at high C-rates. A detailed study of this effect is left to future work.

Finally, the relationship between amplitude and duration of acoustic waveforms (see SM, S6) was consistent with fracture events in

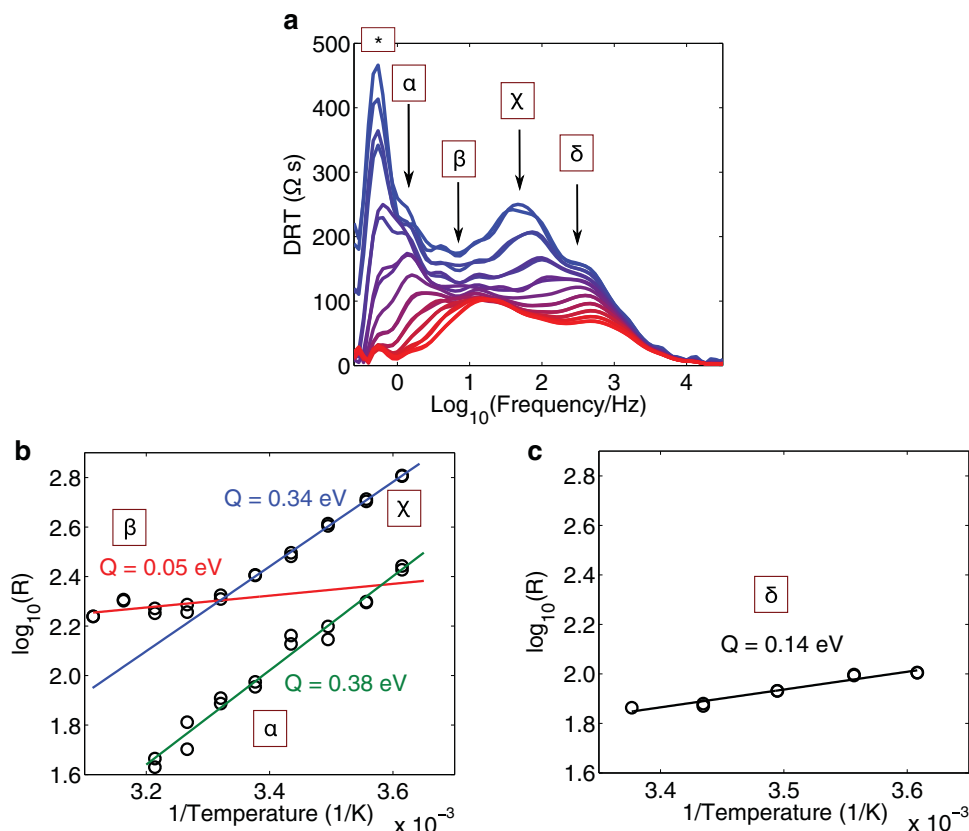


Figure 7. Temperature dependence of electrochemical impedance used to identify underlying mechanisms. a) Impedance contribution separation in Cell B resulting from temperature modulation between 4°C and 48°C at OCV of 3.85 V. Spacing between spectra is ~5°C. b) Activation energy plots for peaks α, β, and χ, as calculated in ZView for Cell C. c) Activation energy plot for peak δ as calculated in ZView for Cell B.

the Si control experiment, as well as with fracture-induced acoustic emissions reported in the literature.¹² From the above analysis and the extensive fracture observed post mortem in the cycled electrode via SEM, we attribute the acoustic emissions to fracture of the LMO particles.

Origin of impedance growth with fracture.—Assignment of physical impedance contributions to DRT peaks.—Accurate assignment of physical impedance contributions to the DRT peaks labeled in Fig. 7a is necessary to identify the mechanism(s) by which fracture affects the impedance. Below, we determine the physical identity of each peak based on control experiments and logical inference.

Peak α: Charge-transfer resistance. Although it is a simplification for LIB chemistry, the classic view of charge-transfer resistance for a one-step, one-electron process gives insight into the expected state-of-charge behavior. From the Butler-Volmer framework, charge transfer resistance R_{ct} is given by⁵⁵

$$R_{ct} = \frac{RT}{Fi_0} \quad [3]$$

where R is the ideal gas constant, T is temperature, F is the Faraday constant and i_0 is the exchange current. The exchange current can be expressed as

$$i_0 = Fk^0 C_O^{*(1-x)} C_R^{*x} \quad [4]$$

where A is the electrochemically active area, k^0 is the standard rate constant, x is the transfer coefficient ($0 < x < 1$) and C_O^* and C_R^* are the concentrations of the oxidized and reduced species in the bulk, respectively. From Eqs. 3 and 4, we can deduce that a minimum in charge-transfer resistance should occur in the potential range of the dominating redox reaction (4.0–4.2 V), and increase as C_O^* or C_R^* becomes small, i.e., as potential moves above or below this range.^{43,45}

This predicted behavior is consistent with peak α in Fig. 8, which increases outside the range of 4.0 V to 4.2 V. Further, this strong thermal activation of 0.38 eV is consistent with that expected for a charge transfer process.^{43,47}

Peaks β and δ: Electronic contact resistance. Multiple authors have reported bulk or surface electronic resistance features in impedance spectra^{31,43,44,47} for LMO and other cathode materials. As with ionic contributions to impedance, electronic contact impedance can exhibit relaxation times observable by EIS due to sufficiently high resistance and capacitance of the corresponding interfaces. The low measured thermal activation energies of 0.05 and 0.14 eV for peaks β and δ, respectively, suggest that the processes associated with these peaks do not involve ionic diffusion through a solid phase. Further-

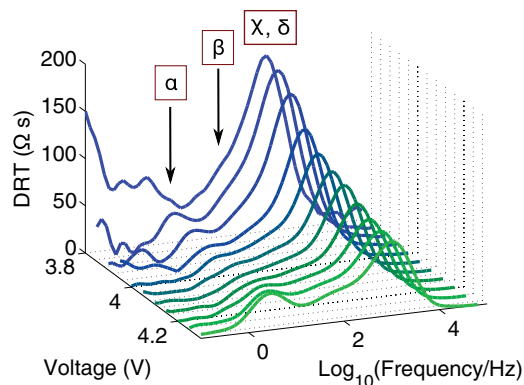


Figure 8. State-of-charge dependence for $\text{Li}_x\text{Mn}_2\text{O}_4$ cell after 1.5 cycles. Potential is decreased from 4.3 V to 3.8 V in increments of 0.05 V.

more, electrical resistance is most likely to appear in electrodes of low carbon content, such as these commercial electrodes with 94.2% active material (< 6% carbon). It is plausible that this contact resistance could arise from the electrode-current collector interface or the interparticle interfaces within the bulk of the cathode. In this case, we assign cathode-current collector resistance to peak δ , and interparticle or particle-carbon resistance to peak β .

We infer this distinction between peaks β and δ by the following control experiment. We fabricated our own “carbon-rich” LMO electrode loaded with 8 wt% carbon and < 5 μm LMO particles, and the resulting cell exhibited an impedance spectrum lacking peak β , as shown and described in SM, S2. However, a temperature-independent peak δ was discovered at high temperature and partially convoluted with a thermally activated peak χ . The contact resistance in this carbon-rich lab-made electrode can be attributed to the segregation of carbon toward the top of the electrode film during tape casting. As shown in the SEM cross-section in SM, S2, contact between the composite electrode and Al foil was primarily dominated by oxide particles with little carbon nearby, while ample carbon was available for interparticle contacts. The occurrence of peak δ and absence of peak β in the carbon-rich film are together consistent with this observation.

Peak χ : LMO surface layer. The thermally activated impedance feature at high frequency is often identified as cathode surface layer or SEI impedance in the literature.^{43,44,56,57} We thus took care to rule out the potential appearance of the Li surface film in the impedance spectrum, which should also be thermally activated and appear at a similar state of charge⁴⁷ (see SM, S3). Along these lines, the LMO cathode was confirmed to be the source of this peak via a three-electrode test (see SM, S4). Separately, an aged cell was opened up and the Li metal and electrolyte were replaced, and it was confirmed that peak χ was not reduced in magnitude by this process (see SM, S5). Finally, the lab-made LMO/Li cell, with one order of magnitude less active material as compared with commercial electrodes, still exhibited a thermally activated peak χ (see SM, S2). The strong presence of peak χ in a cell with significantly less LMO suggests strongly that this peak is attributable to the LMO electrode material.

We can now also consider more specifically the possible sources of this impedance attributed to the LMO particles. The peak still existed in cycled cells maintained below 4.3 V (not shown), for which oxidized electrolyte products are not favored to form on LMO. Moreover, the peak occurred at a highly reproducible time constant from cell to cell, and represented a diffusive component as inferred from the activation energy. Reasonable assignments for this ionic impedance include deposited products of Mn dissolution³⁷ or surface phases (Mn_3O_4) occurring within ~ 10 nm from the surface of cycled LMO.^{58,59} Such surface phases are sensitive to the oxidation state of Mn ions and therefore the state-of-charge of the cell. The altered surface oxidation state of Mn observed in Cell B via XPS is consistent with this hypothesis (see SM, S9), though full confirmation of this impedance contribution deserves future study.

Possible pathways for impedance growth.—As discussed in the Results, the C-rate spikes induced sudden increases in resistance for two impedance features centered at ~ 16 Hz and ~ 600 Hz, which corresponded to peak β and a convolution of peaks χ and δ , respectively. We identified the ~ 16 Hz peak as electrical contact resistance of the bulk (e.g., LMO-LMO contact resistance, such as contact across a crack). We attributed the ~ 600 Hz peak to both current collector contact resistance and an LMO surface layer. To be consistent with these impedance attributions, any causal mechanism postulated to relate fracture and impedance must involve the disruption of electronic conduction, while the role of the LMO surface layer remains admittedly unclear. Here we propose the most likely mechanistic pathways consistent with the observed impedance growth, and highlight uncertainties to be resolved in future work.

First, we must consider why the bulk contact resistance represented by peak β increased concurrently with fracture. As shown in Fig. 1, crack formation can block electron flow by increasing the density of insulating surfaces across which electrons must be transferred.

Electronic transfer across these new surfaces, especially those internal to the particles, is not facilitated by the presence of carbon, so electronic disruption is inevitable in the case of severe degradation. Electronic isolation is perhaps the most widely assumed source of fracture-induced degradation in the literature, and we also consider it to be the most likely explanation for our observations. However, although this mechanism accounts for the growth of peak β with fracture, it does not explain the increase in the peak occurring at 600 Hz.

An alternative explanation for the increase of peak β is the loss of carbon contacts via the dissolution of the LMO active material. Mn dissolution is a well-known effect in LMO, and the loss of material near the carbon contacts could explain the observed increase in contact resistance.^{31,60} However, as this effect occurs at the existing surface and does not require fracture, this impedance growth mechanism should not have high sensitivity to C-rate. Typically, Mn dissolution is a strong function of state-of-charge, particle size, and temperature, and is known to occur during storage without cycling. However, Börner et al.⁶¹ recently observed an increase in Mn dissolution at higher C-rates and attributed it to kinetically imposed local differences in state-of-charge near the LMO surface, where the dissolution reaction takes place.

We therefore find the fracture explanation to be more plausible for the results presented herein. We demonstrated that the growth of this contact resistance was not accelerated significantly by repeated cycling at increased C-rate after the saturation of fracture (see SM, S15). However, the acceleration of a reaction involving the electrolyte is likely also present, and is manifested in the increased ohmic resistance during the C-rate spikes.

The growth of the 600 Hz peak can be explained separately or in tandem with the growth of peak β . In the case of Mn dissolution, undesired phases such as MnF_2 or LiF may deposit on the cathode³⁷ and contribute to surface impedance through peak χ , and fracture may accelerate this deposition by increasing the available surface area for Mn dissolution. Alternatively, if peak χ is due to thin LMO surface phases (such as Mn_3O_4 or tetragonal spinel $\text{Li}_2\text{Mn}_2\text{O}_4$), higher kinetic intrusion into the low-voltage plateau at end of discharge may further alter the Mn oxidation state, affecting the thickness of these phases. In that case, recovery should be expected after a return to normal cycling, but it is unclear whether this recovery would occur within the time scale of these experiments. Further investigations of the effect of C-rate spikes and concurrent fracture over longer time scales should facilitate increased understanding of fracture effects on capacity and impedance for > 100s of cycles.

Over the past decade, the battery community has made great strides toward understanding the conditions for electrochemical shock, and design methods are already in place to reduce the occurrence of fracture in active electrode materials. However, the connection between electrode material fracture and electrochemical performance is conveyed chiefly via models, schematics, and assumptions that require further experimental evidence. By triggering controlled fracture events through extended electrochemical cycling, we have presented a methodical approach to measure a temporal correlation between fracture and changes in electrochemical impedance, and have thereby identified plausible mechanisms by which fracture promotes impedance growth in this model system.

Conclusions

Here we implemented an electrochemical shock-based C-rate spike approach to trigger discrete fracture events during repeated cycling of $\text{Li}_x\text{Mn}_2\text{O}_4/\text{Li}$ cells. Increased cycling rates during the C-rate spikes led to increased acoustic emissions, which we interpreted as C-rate dependent fracture of the active LMO particles in the positive composite electrode. We confirmed the occurrence of extensive particle fracture by electron microscopy image comparison of cycled and uncycled $\text{Li}_x\text{Mn}_2\text{O}_4$ electrodes. Concurrently with the fracture triggered by C-rate spikes, we observed impedance growth corresponding to at least two physical contributions. By distribution of relaxation times

analysis and several control experiments, we identified one impedance contribution as the electronic contact resistance within the bulk of the cathode. We hypothesize that this impedance growth is caused by cracks disrupting electronic flow within the particles. The other source of impedance growth is attributed to either current collector resistance or to thin secondary phases on the surface of LMO. Knowledge of this correlation between fracture and electrochemical performance in $\text{Li}_x\text{Mn}_2\text{O}_4$ and other electrode materials is critical for understanding the effect of fracture in LIBs, and ultimately will aid in determining design criteria for energy storage devices with increased durability and lifetime.

Acknowledgments

We gratefully acknowledge support from the US Department of Energy's Office of Basic Energy Science for the Chemomechanics of Far-From-Equilibrium Interfaces (COFFEI) small group, through award number DE-SC0002633 (J. Vetrano, Program Manager). This work made use of the Shared Experimental Facilities supported in part by the MRSEC Program of the National Science Foundation under award number DMR-1419807. F. P. McGrogan also acknowledges the MIT Martin Fellowship for Sustainability. We also thank B. Sheldon (Brown University) and T. Swamy (MIT) for helpful discussions.

References

- J. B. Goodenough and K.-S. Park, *J. Am. Chem. Soc.*, **135**, 1167 (2013).
- N. Nitta, F. Wu, J. T. Lee, and G. Yushin, *Mater. Today*, **18**, 252 (2015).
- R. Narayanan, M. M. Joglekar, and S. Inguva, *J. Electrochem. Soc.*, **160**, A125 (2013).
- K. E. Aifantis, T. Huang, S. A. Hackney, T. Sarakonsri, and A. Yu, *J. Power Sources*, **197**, 246 (2012).
- X. Hao, X. Lin, W. Lu, and B. M. Bartlett, *ACS Appl. Mater. Interfaces*, **6**, 10849 (2014).
- A. Mukhopadhyay and B. W. Sheldon, *Prog. Mater. Sci.*, **63**, 58 (2014).
- C.-F. Chen, P. Barai, and P. P. Mukherjee, *J. Electrochem. Soc.*, **161**, A2138 (2014).
- J. A. Gilbert, I. A. Shkrob, and D. P. Abraham, *J. Electrochem. Soc.*, **164**, A389 (2017).
- R. Deshpande, M. Verbrugge, Y.-T. Cheng, J. Wang, and P. Liu, *J. Electrochem. Soc.*, **159**, A1730 (2012).
- W. H. Woodford, W. C. Carter, and Y.-M. Chiang, *Energy Environ. Sci.*, **5**, 8014 (2012).
- K. Sawai, K. Yoshikawa, H. Tomura, and T. Ohzuku, *Prog. Batter. Batter. Mater.*, **17**, 201 (1998).
- K. Rhodes, N. Dudney, E. Lara-Curzio, and C. Daniel, *J. Electrochem. Soc.*, **157**, A1354 (2010).
- P. Barai and P. P. Mukherjee, *J. Electrochem. Soc.*, **161**, F3123 (2014).
- K. An, P. Barai, K. Smith, and P. P. Mukherjee, *J. Electrochem. Soc.*, **161**, A1058 (2014).
- P. Yan, J. Zheng, M. Gu, J. Xiao, J.-G. Zhang, and C.-M. Wang, *Nat. Commun.*, **8**, 14101 (2017).
- D. Wang, X. Wu, Z. Wang, and L. Chen, *J. Power Sources*, **140**, 125 (2005).
- T. A. Arunkumar and A. Manthiram, *Electrochem. Solid-State Lett.*, **8**, A403 (2005).
- J. Liu and A. Manthiram, *J. Phys. Chem. C*, **113**, 15073 (2009).
- F. Hao and D. Fang, *J. Electrochem. Soc.*, **160**, A595 (2013).
- G. T.-K. Fey, C.-Z. Lu, and T. P. Kumar, *J. Power Sources*, **115**, 332 (2003).
- J. Liu and A. Manthiram, *J. Electrochem. Soc.*, **156**, A833 (2009).
- A. Manthiram, K. Chemelewski, and E.-S. Lee, *Energy Environ. Sci.*, **7**, 1339 (2014).
- W. H. Woodford, Y.-M. Chiang, and W. C. Carter, *J. Electrochem. Soc.*, **160**, A1286 (2013).
- R. A. Huggins and W. D. Nix, *Ionics*, **6**, 57 (2000).
- D. J. Miller, C. Proff, J. G. Wen, D. P. Abraham, and J. Bareño, *Adv. Energy Mater.*, **3**, 1098 (2013).
- J. G. Swallow, W. H. Woodford, F. P. McGrogan, N. Ferralis, Y.-M. Chiang, and K. J. Van Vliet, *J. Electrochem. Soc.*, **161**, F3084 (2014).
- W. H. Woodford, Y.-M. Chiang, and W. C. Carter, *J. Electrochem. Soc.*, **157**, A1052 (2010).
- S. K. Soni, B. W. Sheldon, X. Xiao, A. F. Bower, and M. W. Verbrugge, *J. Electrochem. Soc.*, **159**, A1520 (2012).
- K. Zhao, M. Pharr, J. J. Vlassak, and Z. Suo, *J. Appl. Phys.*, **108**, 073517 (2010).
- J. Vetter, P. Novák, M. R. Wagner, C. Veit, K.-C. Möller, J. O. Besenhard, M. Winter, M. Wohlfahrt-Mehrens, C. Vogler, and A. Hammouche, *J. Power Sources*, **147**, 269 (2005).
- D. H. Jang, Y. J. Shin, and S. M. Oh, *J. Electrochem. Soc.*, **143**, 2204 (1996).
- Y. Liu, X. Li, H. Guo, Z. Wang, Q. Hu, W. Peng, and Y. Yang, *J. Power Sources*, **189**, 721 (2009).
- D. Aurbach, B. Markovsky, Y. Talyossef, G. Salitra, H.-J. Kim, and S. Choi, *J. Power Sources*, **162**, 780 (2006).
- T. Waldmann, N. Ghanbari, M. Kasper, and M. Wohlfahrt-Mehrens, *J. Electrochem. Soc.*, **162**, A1500 (2015).
- R. Wang, X. Li, Z. Wang, and H. Guo, *J. Solid State Electrochem.*, **20**, 19 (2016).
- O. K. Park, Y. Cho, S. Lee, H.-C. Yoo, H.-K. Song, and J. Cho, *Energy Environ. Sci.*, **4**, 1621 (2011).
- N. P. W. Pieczonka, Z. Liu, P. Lu, K. L. Olson, J. Moote, B. R. Powell, and J.-H. Kim, *J. Phys. Chem. C*, **117**, 15947 (2013).
- C.-H. Lu and S.-W. Lin, *J. Mater. Res.*, **17**, 1476 (2002).
- J. Sheth, N. K. Karan, D. P. Abraham, C. C. Nguyen, B. L. Lucht, B. W. Sheldon, and P. R. Guduru, *J. Electrochem. Soc.*, **163**, A2524 (2016).
- M. M. Thackeray, Y. Shao-Horn, A. J. Kahaian, K. D. Kepler, E. Skinner, J. T. Vaughey, and S. A. Hackney, *Electrochem. Solid-State Lett.*, **1**, 7 (1998).
- Y. Shao-Horn, S. A. Hackney, A. J. Kahaian, K. D. Kepler, E. Skinner, J. T. Vaughey, and M. M. Thackeray, *J. Power Sources*, **81-82**, 496 (1999).
- M. Nishizawa, T. Ise, H. Koshika, T. Itoh, and I. Uchida, *Chem. Mater.*, **12**, 1367 (2000).
- S. Kumar, P. K. Nayak, K. S. Hariharan, and N. Munichandraiah, *J. Appl. Electrochem.*, **44**, 61 (2014).
- Q.-C. Zhuang, T. Wei, L.-L. Du, Y.-L. Cui, L. Fang, and S.-G. Sun, *J. Phys. Chem. C*, **114**, 8614 (2010).
- M. Mohamedi, M. Makino, K. Dokko, T. Itoh, and I. Uchida, *Electrochim. Acta*, **48**, 79 (2002).
- A. Jossen, *J. Power Sources*, **154**, 530 (2006).
- J. Illig, M. Ender, T. Chrobak, J. P. Schmidt, D. Klotz, and E. Ivers-Tiffée, *J. Electrochem. Soc.*, **159**, A952 (2012).
- H. Schichlein, A. C. Müller, M. Voigts, A. Krügel, and E. Ivers-Tiffée, *J. Appl. Electrochem.*, **32**, 875 (2002).
- A. L. Smirnova, K. R. Ellwood, and G. M. Crosbie, *J. Electrochem. Soc.*, **148**, A610 (2001).
- J. P. Schmidt, T. Chrobak, M. Ender, J. Illig, D. Klotz, and E. Ivers-Tiffée, *J. Power Sources*, **196**, 5342 (2011).
- K. Xu, *Chem. Rev.*, **114**, 11503 (2014).
- X. Q. Yang, X. Sun, S. J. Lee, J. McBreen, S. Mukerjee, M. L. Daroux, and X. K. Xing, *Electrochem. Solid-State Lett.*, **2**, 157 (1999).
- D. Aurbach, M. D. Levi, E. Levi, H. Teller, B. Markovsky, G. Salitra, U. Heider, and L. Heider, *J. Electrochem. Soc.*, **145**, 3024 (1998).
- W. H. Woodford, W. C. Carter, and Y.-M. Chiang, *J. Electrochem. Soc.*, **161**, F3005 (2014).
- A. J. Bard and L. R. Faulkner, *Electrochemical Methods: Fundamentals and Applications*, 2nd ed., p. 102, John Wiley & Sons, New York (2001).
- S. S. Zhang, K. Xu, and T. R. Jow, *J. Electrochem. Soc.*, **149**, A1521 (2002).
- M. Hirayama, H. Ido, K. S. Kim, W. Cho, K. Tamura, J. Mizuki, and R. Kanno, *J. Am. Chem. Soc.*, **132**, 15268 (2010).
- C. D. Amos, M. A. Roldan, M. Varela, J. B. Goodenough, and P. J. Ferreira, *Nano Lett.*, **16**, 2899 (2016).
- D. Tang, Y. Sun, Z. Yang, L. Ben, L. Gu, and X. Huang, *Chem. Mater.*, **26**, 3535 (2014).
- J. Park, J. H. Seo, G. Plett, W. Lu, and A. M. Sastry, *Electrochem. Solid-State Lett.*, **14**, A14 (2011).
- M. Bömer, S. Klamor, B. Hoffmann, M. Schroeder, S. Nowak, A. Würsig, M. Winter, and F. M. Schappacher, *J. Electrochem. Soc.*, **163**, A831 (2016).